Virtual synchronous generators for voltage synchronization of a hybrid PV-diesel power system

Ahmed Belila[a,c], Yassine Amirat[b], Mohamed Benbouzid[c,e,*], El Madjid Berkouk[d], Gang Yao[e]

[a] Ecole Militaire Polytechnique, UER ELT, 16111 Algiers, Algeria
[b] ISEN Yncréa Ouest Brest, UMR CNRS 6026 IRDL, 29200 Brest, France
[c] University of Brest, UMR CNRS 6026 IRDL, 29238 Brest, France
[d] Ecole Nationale Polytechnique, LCP-lab, 16000 Algiers, Algeria
[e] Shanghai Maritime University, Shanghai, China

ABSTRACT

To ensure the synchronization process in a hybrid PV-Diesel generation system parallel topology, a phase-locked loop is generally used to estimate the angular frequency of the point of common coupling. However, the DG rotor inaccessibility imposes its operation mode as a master. This will therefore affect the system overall stability since the phase-locked loop is affected by oscillations, which are predicted by the power-angle curve concept interacting with the DG rotary inertia. In this context, this paper proposes a new control strategy based on virtual synchronous generators for a stand-alone PV-Diesel hybrid generation system to synchronize the output voltages without a phase-locked loop, while correcting the diesel generator rotor initial position and ensuring power sharing between the two sources, according to a desired power ratio. To prove the effectiveness of the proposed control strategy, simulation and experiments are carried out. The achieved results clearly illustrated the feasibility and the improvement brought by the proposed virtual synchronous generators-based control strategy.

1. Introduction

Various hybrid power generation systems based on diesel generators have been used widely in several applications. The integration of renewable energy sources (RES) such as PV and wind into this type of hybrid energy system have been a focal point, while the synchronization process of these hybrid systems, connected to the main utility grid through Voltage Source Inverter (VSI), has been indexed as one of the major stability issue.

To ensure the synchronization process a phase-locked loop (PLL) is generally used to estimate the angular frequency of the point of common coupling (PCC). However, the DG rotor inaccessibility imposes a slave operation mode of the VSI and a master operation mode of the DG as illustrated by Fig. 1.

Since a stand-alone microgrid with a small system inertia is vulnerable to the output power fluctuations of intermittent renewable generation systems [1], the DG master operation mode entails the following drawbacks:

- The PLL stability is affected by the DG transients [2].
- Oscillations appearance during the sources synchronization. These

oscillations are predicted from the power-angle curve concept interacting with the DG rotary inertia. This will therefore affect the overall system stability [3].

In this context, this paper proposes a new control strategy based on Virtual Synchronous Generators (VSG) for a hybrid PVG-DG power system in a stand-alone context. This control concept consists in emulating the VSI operation by a synchronous machine. This makes it possible to ensure synchronization at PCC without using a PLL [4] and limits the above-mentioned drawbacks [5].

In the literature, the VSG concept was proposed and studied by many researchers quite recently [6]. Main research works were mainly focused towards its application and the stability analysis [7–9]. The VSG concept has been well investigated with different practical implementations [10–12]. Majority of the carried out investigations were focused on the implementation of the VSG concept for parallel VSIs in microgrids and dealing with the transition between grid-connected to islanded modes [7,13,14]. In [7], an enhanced VSG control without PLL was proposed for multiple parallel inverters and an accurate small-signal model of the multiple parallel VSGs system was derived for system analysis and parameter design. In the same context, a very

---

Nomenclature		E_0	Stator winding emf
		ω	Electrical angular speed
PVG-DG	PV Generator-Diesel Generator	ω_N	Rated electrical angular speed
RES	Renewable Energy Sources	ω_m	Mechanical speed
VSG	Virtual Synchronous Generators	J	Rotational inertia
PLL	Phase-Locked Loop	θ	Electrical angle
PCC	Point of Common Coupling	I_{ph}	Photocurrent
AVR	Automatic Voltage Regulation	I_0	Diode saturation current
VEV	Virtual Excitation Voltage	q	Coulomb constant
PI	Proportional Integral	k	Boltzmann constant
MPPT	Maximum Power Point Tracking	G	Global insulation
$T_m(T_e)$	Mechanical (electromagnetic) torque	SOC	State of Charge
$P_m(P_e)$	Mechanical (electromagnetic) power	SOC_0	Initial State of Charge

interesting review of active and reactive power sharing strategies in hierarchical controlled microgrids has been presented in [15] and an active and reactive power sharing control strategy for VSGs in microgrid in [16]. In [17], an enhanced VSG control is proposed, where oscillations damping and proper transient active power sharing are achieved by adjusting the virtual stator reactance based on a state-space analysis. In [13], it is proposed a power decoupling method based on a decoupling matrix in the VSG control unit. This method is based on the linearized power transfer model. In [18], it was proposed an improved dual droop control (for the VSI and the DC side energy storages) to ensure the VSG functions and to achieve power management.

To achieve higher stability in a microgrid including a small DG, a master operating mode is required for the VSI. However and as it was previously discussed, the access to the DG rotor and its initial position, present a challenging task to impose a slave mode for the DG. To address this issue, this paper proposes a new control strategy based on VSG for a hybrid PVG-DG power system including an Energy Storage System (ESS) in a stand-alone context, to synchronize the output voltages without a PLL, while correcting the diesel generator rotor initial position and also the ensuring power sharing between the two power sources according to a desired power ratio. It should be mentioned here that the stability issue is not addressed in this paper as the considered micro grid is not subject to disturbances inducing high oscillations [19,20].

The paper is organized as follows: The system structure and modeling is described in Section 2. In Section 3, the principle of the proposed synchronization method and power sharing control is presented. Simulation results are presented in Section 4, while the experimental ones are given in Section 5. Section 6 concludes the paper.
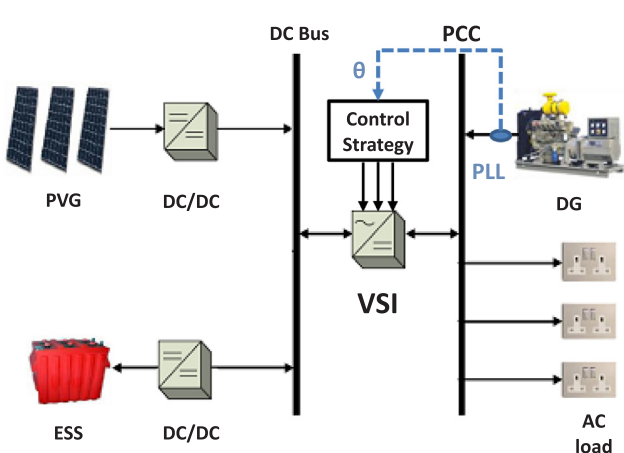
2. System structure and modeling

Fig. 2, shows the structure of the parallel hybrid PVG-DG power system using VSG control. The PVG is connected to the DC bus through a boost converter controlled by an MPPT Perturb and Observ (P&O) strategy. The DG is connected to the AC bus and the energy storage system (ESS) is designed for regulating the DC bus voltage in order to supply or absorb insufficient/surplus power generated by PVG and/or DG. The AC bus of the studied system, can be simplified as described in Fig. 3. It consists in connecting in parallel two synchronous generators, a real synchronous generator (RSG), which represents the (DG), and a virtual synchronous generator (VSG)(DG), which represents the VSI associated to the PVG, and ESS sources.

2.1. Real synchronous generator model

In Fig. 3a, the DG model is illustrated in a block diagram form. This model is widely used and well-describes the dynamic behavior of small DG sets [21]. The valve actuator and the diesel engine are represented by first-order lags, with time constants T_v and T_d, respectively. In this model, the mechanical input of the synchronous generator is the PI controller output. The relationship between the electromagnetic torque T_m and the angular velocity ω_m of the DG rotor can be expressed by Eq. (1), where J is the combined moment of inertia of the diesel engine and the synchronous generator.

$$J\frac{d\omega_m}{dt} = T_m - T_e \tag{1}$$

It can be noted from Eq. (1) that the system frequency depends on the DG rotational speed and its variation is inversely proportional to the system inertia J. This highlight the fact that DGs with small inertias are vulnerable to load changes as discussed in the Introduction Section
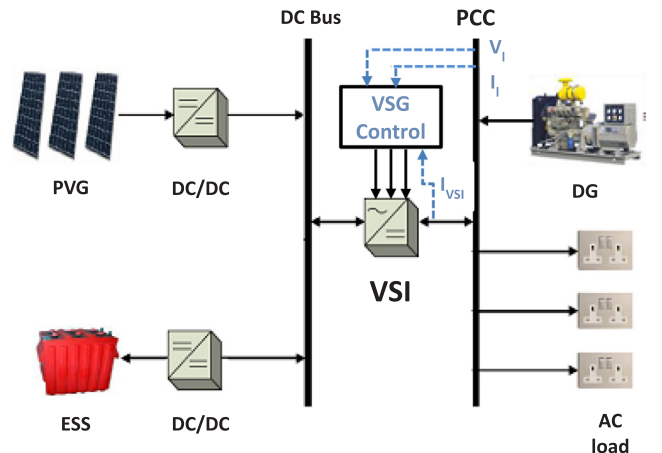

Fig. 1. Conventional synchronization process with PLL.

Fig. 2. Proposed synchronization Process without PLL.
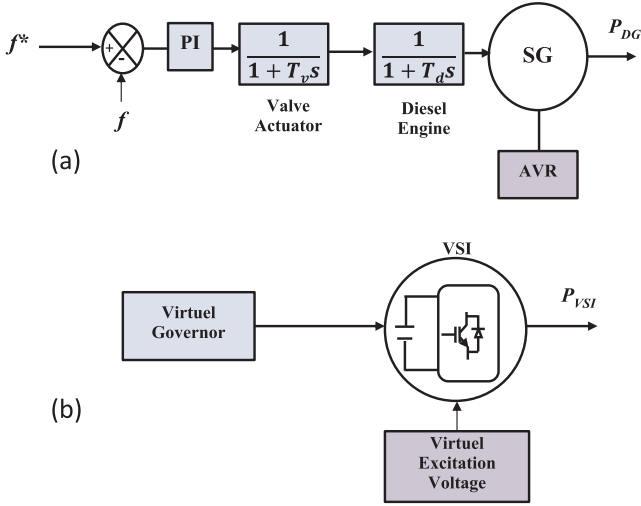
Fig. 3. (a) DG block diagram, (b) VSI block diagram.

[22].

The nominal output voltages of SG are maintained constant by an Automatic Voltage Regulation (AVR) system [21]. The SG and AVR models are referred in the mathworks toolbox user guide.

2.2. Virtual synchronous generator model

According to the VSG principle, the PVG and the ESS can be equivalent to a prime mover (Fig. 3), and the classical three-phase voltage-source inverter VSI will operate as a synchronous generator. In this case, the relevant control strategies and theoretical analysis of a real synchronous generator can be effectively transferred into the studied microgrid [23].

Similarly, the second-order model is a typical one for a VSI [24,25]. As shown in Fig. 3b, to emulate the DG diesel engine and the AVR system, a virtual governor and a virtual excitation system are respectively used. The mechanical and the electrical parts of VSI are described by the following equations system [5,10,12]:

$$
\begin{cases}
T_m - T_e - D\Delta\omega = \frac{P_m}{\omega} - \frac{P_e}{\omega} - D\Delta\omega = J\frac{d\omega}{dt} \\
\omega = \frac{d\theta}{dt}, \Delta\omega = \omega - \omega_B \\
E_0 = U_s + I(r_a + jx_s)
\end{cases}
\tag{2}
$$

where T_m and T_e are the mechanical torque of the synchronous generator rotor shaft input from a prime mover and the stator electromagnetic torque, respectively; D is the damping coefficient used to represent the prime mover damping characteristics; ω is the actual electrical angular velocity and ω_B is rated one. With the assumption of a pole pairs number of 1, mechanical angular velocity $\omega_m = \omega$; P_m and P_e are the mechanical power and electromagnetic power, respectively; J and θ are the rotational inertia and electrical angle, respectively; E_0 is the three-phase stator winding emf; U_S and I are the stator voltage and current, respectively, and r_a and x_s are respectively the armature resistance and synchronous reactance.

2.2.1. VSI model

The schematic diagram of a three-phase voltage source inverter VSI is shown in Fig. 4. It comprises a voltage source at its input and a current source at its output. The connection between these two sources is periodically done through bidirectional current switches.

Assuming that F_{ij} represents the connection function for each switch (K_{ij}):

$$
\begin{cases}
Fij = 1 \rightarrow if: Ki1 = 1 \\
Fij = 0 \rightarrow if: Ki1 = 0
\end{cases}
\tag{3}
$$

Thus, the output voltages of VSI, can be expressed in the following matrix form:

$$
\begin{bmatrix} V_{an} \\ V_{bn} \\ V_{cn} \end{bmatrix} = \frac{1}{3}V_{dc} \begin{bmatrix} 2 & -1 & -1 \\ -1 & 2 & -1 \\ -1 & -1 & 2 \end{bmatrix} \begin{bmatrix} F_{11} \\ F_{21} \\ F_{31} \end{bmatrix}
\tag{4}
$$

2.2.2. PVG model

The photovoltaic cell is the main part of a PV system. A single-diode model can be used to simulate silicon photovoltaic cells (Fig. 5(a)). A photovoltaic cell is a nonlinear device, which can be modeled by a current source generating the photo current I_{ph}, a diode, a series-resistance taking into account the internal resistance R_S, and a parallel resistance R_P representing the leakage current [26].

$$
I_{cel} = I_{ph} - I_0 \left(e^{\left(\frac{V_{pv} + R_s I}{aV_T}\right)} - 1 \right) - \left(\frac{V_{pv} + R_s I}{R_P} \right)
\tag{5}
$$

With the thermal potential s given by:

$$
V_T = \frac{n_s kT}{q}
\tag{6}
$$

where I_{cel} and V_{pv} are the output current and voltage of the PV cell, respectively, I_0 is the reverse saturation current, a is the ideality factor, T is the PV temperature (K) and k is the Boltzmann constant [2].

For a PVG containing n_s and n_p panels in series and in parallel, respectively, the output current I_{PVG} is given by:

$$
I_{PVG} = n_p I_{ph} - n_p I_0 \left(e^{\left(\frac{V_{pv} + R_{sG} I}{an_s V_T}\right)} - 1 \right) - \frac{V_{pv} + R_{sG} I_{pv}}{R_{pG}}
\tag{7}
$$

Where:

$$
\begin{cases}
R_{sG} = \frac{n_s R_s}{n_p} \\
R_{sP} = \frac{n_s R_p}{n_p}
\end{cases}
\tag{8}
$$

2.2.3. ESS model

For energy conversion, a simple modeling approach has been adopted for the batteries of ESS [27]. In this model, the battery equivalent circuit is illustrated by Fig. 5(b), where the battery voltage is given by:

$$
V_{bat} = E_0 - R_{bat} i - V_{C_{bat}}
\tag{9}
$$

The battery state of charge (SOC) is given by [1],[15][16]:

$$
SOC(t) = SOC(0) - \frac{1}{C_{bat}} \int_0^t i(t)dt
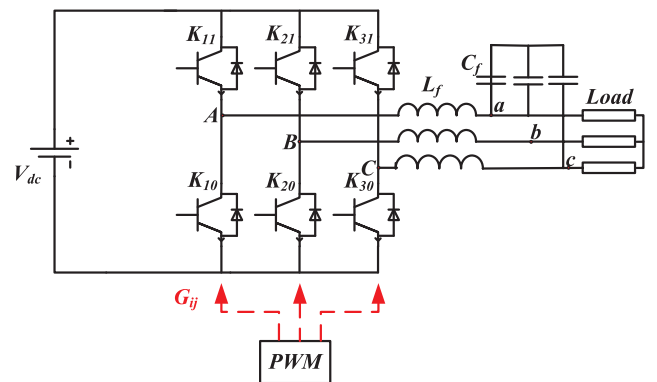\tag{10}
$$

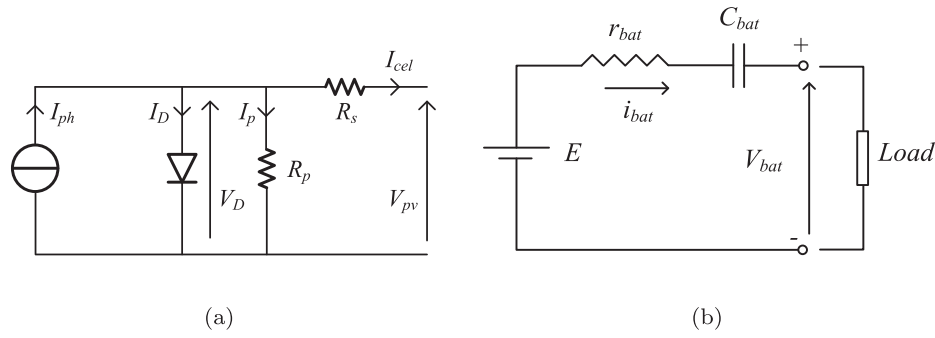
Fig. 4. VSI topology.

Fig. 5. (a) PVG model. (b) ESS model.

3. Proposed synchronisation process and power sharing method

When the VSI and the DG are interconnected, the stator voltages and currents of the real and virtual generators must have the same frequency and the rotor mechanical speed of each is synchronized to this frequency. Therefore, interconnected synchronous generators rotors must be in synchronism.

3.1. Synchronisation process

Fig. 6 shows the equivalent circuit and the phasor diagram of the interconnected synchronous generators before synchronization, where V_{VSI} and V_{DG} represent the VSI and DG output voltage amplitudes, respectively. V_1 and V_2 are the virtual and real electromotive force, respectively; (δ_1, δ_2) are the phase angles difference between (V_1, V_{VSI}) ,

and (V_2, V_{DG}), respectively. δ_0 is the phase-shift between V_{VSI}, V_{DG}; α is the rotor initial phase of the DG; (x_1, r_1) are the VSI filter reactance and resistance, respectively; and (x_2, r_2) are the DG stator reactance and resistance, respectively.

To ensure the two sources synchronization, the two output voltages V_{VSI} and V_{DG}, must be superimposed thus imposing a zero phase-shift $\delta_0 = 0$.

From the phasor diagram in Fig. 6(b), it is clear that under no-load operation, the synchronism ($\delta_0 = 0$) can be ensured only by the correction of the rotor initial position (α). In this mode, the correction of α is determined in relation to (x_1, r_1) and (x_2, r_2), as it will be latter detailed.

The active and reactive powers of the VSI and DG can be written as follows [16,28]:
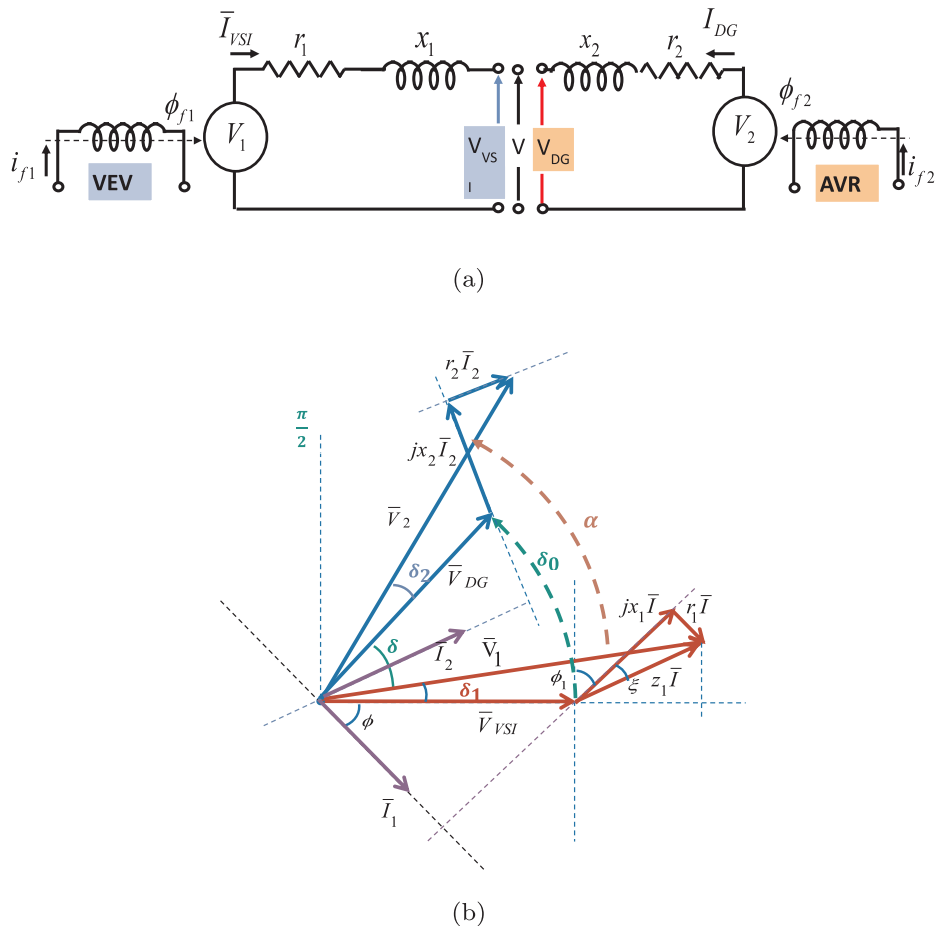

(a)

(b)

Fig. 6. Simplified connection of the two sources before synchronization: (a) Equivalent circuit. (b) Phasor diagram.

$$\begin{cases} P_{VSI} = \frac{V_1}{(r_1)^2 + (x_1)^2}(r_1(V_1 - V_{VSI}cos\delta_1) + x_1 V_{VSI}sin\delta_1)) \\ Q_{VSI} = \frac{V_1}{(r_1)^2 + (x_1)^2}(-r_1 V_{VSI}sin\delta_1 + x_1(V_1 - V_{VSI}cos\delta_1)) \end{cases} \quad (11)$$

$$\begin{cases} P_{DG} = \frac{V_2}{(r_2)^2 + (x_2)^2}(r_2(V_2 - V_{DG}cos\delta_2) + x_2 V_{DG}sin\delta_2)) \\ Q_{DG} = \frac{V_2}{(r_2)^2 + (x_2)^2}(-r_2 V_{DG}sin\delta_2 + x_2(V_2 - V_{DG}cos\delta_2)) \end{cases} \quad (12)$$

To ensure the two sources synchronization under loaded operation, a zero phase-shift ($\delta_0 = 0$) must be imposed via the correction of the rotor initial position ($\alpha_i \neq 0$), which is determined according to the desired power ratio between the two sources (R_i).

Fig. 7 shows the equivalent circuit and the phasor diagram under load operation, of the interconnected synchronous generators after synchronization, where the two output voltages V_{VSI} and V_{DG} are superimposed ($V = V_{VSI} = V_{DG}$).

From Eqs. (11) and (12), the active and reactive powers that the VSI and DG will deliver to the PCC under load operation can be rewritten as follows:

$$\begin{cases} P_{VSI} = \frac{V_1}{(r_1)^2 + (x_1)^2}(r_1(V_1 - Vcos\delta_1) + x_1 Vsin\delta_1)) \\ Q_{VSI} = \frac{V_1}{(r_1)^2 + (x_1)^2}(-r_1 Vsin\delta_1 + x_1(V_1 - Vcos\delta_1)) \end{cases} \quad (13)$$

$$\begin{cases} P_{DG} = \frac{V_2}{(r_2)^2 + (x_2)^2}(r_2(V_2 - Vcos\delta_2) + x_2 Vsin\delta_2)) \\ Q_{DG} = \frac{V_2}{(r_2)^2 + (x_2)^2}(-r_2 Vsin\delta_2 + x_2(V_2 - Vcos\delta_2)) \end{cases} \quad (14)$$

Note here that, since the two sources are directly connected to the PCC, the lines impedances r_{L1}, x_{L1} and r_{L2} x_{L2} after the (PCC) are included in P_{load} and Q_{load}.

In this paper, the P/f and Q/V droop control strategies will be discussed for the considered hybrid PVG-DG-ESS system, under the assumption that the line impedance is approximately inductive. This assumption is based on the fact that the line impedance of the virtual and real stators winding is approximately inductive. Indeed, the resistive part of each stator winding can be neglected compared to the inductive one and the power angles δ_1 and δ_2 in such lines are small. It can then be assumed that: $sin\delta_1 = \delta_1$, $sin\delta_2 = \delta_2$ and ($cos\delta_1 = cos\delta_2 = 1$). In addition, when the two sources are synchronized at PCC (Fig. 7(b)), we have:

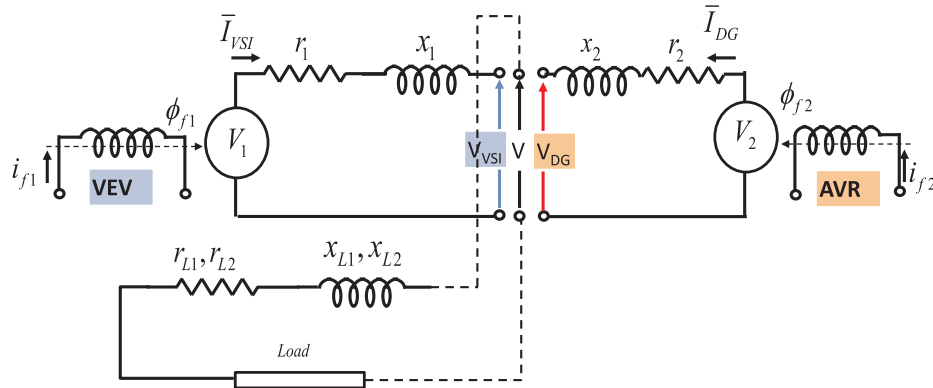$$\begin{cases} \delta_2 = \delta_1 + \alpha \\ V_{VSI} = V_{DG} = V \end{cases} \quad (15)$$

Therefore allowing rewriting Eqs. (13) and (14) as:

$$\begin{cases} P_{VSI} = \frac{V_1 V \delta_1}{x_1} \\ Q_{VSI} = \frac{V_1(V_1 - V)}{x_1} \end{cases} \quad (16)$$
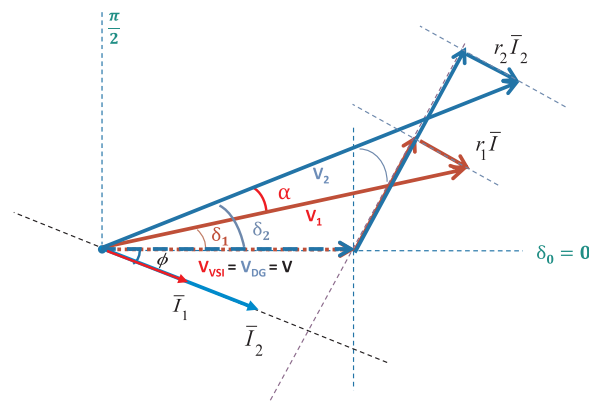
$$\begin{cases} P_{DG} = \frac{V_2 V (\delta_1 + \alpha)}{x_2} \\ Q_{DG} = \frac{V_2(V_2 - V)}{x_2} \end{cases} \quad (17)$$

The following power ratio can therefore be deduced.

$$\begin{cases} R_P = \frac{P_{VSI}}{P_{DG}} = \frac{V_1 x_2}{V_2 x_1} \frac{\delta_1}{\delta_1 + \alpha} \\ R_Q = \frac{Q_{VSI}}{Q_{DG}} = \frac{x_2}{x_1} \frac{V_1}{V_2} \frac{V_1 - V}{V_2 - V} \end{cases} \quad (18)$$

(a)

(b)

Fig. 7. Simplified connection of the two sources after synchronization: (a) Equivalent circuit. (b) Phasor diagram.

where, R_P and R_Q are the desired active and reactive power ratios between the two sources, respectively. These relations show that it is possible to ensure the synchronization between the two energy sources by a judicious control of the active and reactive power delivered by the VSI. It particularly highlights a very interesting method to correct the rotor initial position α of the DG, since the exchanged active and reactive powers can be fixed beforehand through the control. Indeed, the initial angle of the DG rotor can be expressed as follows:

$$\alpha = \delta_1 \left(\frac{V_1}{V_2} \frac{x_2}{x_1} \frac{1}{R_P} - 1 \right) \tag{19}$$

This angle, which can be fixed beforehand mainly according to the VSI power angle δ_1, the ratio between the reactances of the real and the virtual stator winding $\frac{x_2}{x_1}$, the desired active power ratio R_P and the ratio between the virtual and real electromotive force $(\frac{V_1}{V_2})$ which is corresponding to the desired reactive power ratio R_Q. Indeed, Eq. (19) can be expressed as a function of R_P and R_Q as follows:

$$\alpha = \delta_1 \left(\frac{R_Q}{R_P} \cdot \frac{V_2 - V}{V_1 - V} - 1 \right) \tag{20}$$

This relation gives rise to two distinguished correction of the rotor initial position:

- When the active and reactive power ratios between the two sources are the same $R_P = R_Q$. In this case the desired power ratio is $(R = R_P = R_Q)$ and whatever its value, a zero angle of the rotor initial position must be imposed ($\alpha = 0$).
- When the active and reactive power ratios between the two sources are different $R_P \neq R_Q$. In this case, for each value of (R_P, R_Q), a phase-shift between the two sources must be imposed through the rotor initial position ($\alpha_{pq} \neq 0$).

It is clear from Eq. (20), that unlike the first case, the second case corresponding to $(R_P \neq R_Q)$, requires a prior identification of the value of δ_1, to impose a rotor initial position ($\alpha_{pq} \neq 0$).

3.2. VSG-based control strategy

To properly share the active and reactive powers between the two sources, the desired power ratios R_P and R_Q should be equally designed, as it has been above-discussed. Therefore, the proposed VSG-based control scheme, shown in Fig. 8, can be subdivided on in six control parts: Power calculation, Virtual inertia, Virtual Governor, Virtual excitation system, References voltages generation and DG rotor initial position correction.

3.2.1. Power calculation

Equations describing the instantaneous active and reactive powers are expressed, according to the output voltages and currents taken from the LC filter interface measurements, as:

$$\begin{cases} P(t) = v_a i_a + v_b i_b + v_c i_c \\ Q(t) = \frac{1}{\sqrt{3}} [(v_b - v_c)i_a + (v_c - v_a)i_b + (v_a - v_b)i_c] \end{cases} \tag{21}$$

3.2.2. Virtual inertia

The emulation of a rotating inertia is the main difference between the VSG control strategy and the conventional droop control [29]. The virtual inertia control scheme, shown in part 1 of Fig. 9, is based on a conventional swing equation (Eq. (2)), representing the inertia and damping of a traditional synchronous generator, where the acceleration of the inertia is determined by the power balance between the virtual mechanical input power P_m, the measured electrical power flowing from the VSI output P_{VSI}, and the damping effect which is defined by the damping coefficient D and the difference between the rotor angular frequency w and its rated value w_n.

3.2.3. Virtual governor system

To emulate the DG speed governor characteristics, the traditional frequency droop control is used. As shown in Part 2 of Fig. 9, the virtual mechanical input power P_m of the virtual inertia block is given by the sum of the active load power reference P_{L1}, and the frequency droop effect, where k_p is the frequency adjustment coefficient [30]. The active load power reference P_{L1} can be determined as a function of the active power required by the load P_L and R_P, as follows:

$$P_{L1} = P_L \left(\frac{R_P}{R_P + 1} \right) \tag{22}$$

The droop controllers P/f equation is given as follows, where k_p is the frequency adjustment coefficient [31]:

$$P_m - P_{L1} = k_p(\omega^* - \omega_{VSI}) \tag{23}$$

However, and especially for the practical implementation when a low-pass filter (LPF) need to be used to filter the averaged active and reactive output powers, Eq. (23) can be rewritten as follows:

$$P_m - P_{L1} = \left(\frac{m}{\tau p + 1} \right)(\omega^* - \omega_{VSI}) \tag{24}$$

where τ is the time-constant of the low-pass filter and m is the P/w droop coefficient which, can be chosen according to the maximum and minimum values of the allowable angular frequency (ω_{max}, ω_{min}) and the maximum and minimum capacities of the active power (P_{max}, P_{min}) as follows [32]:
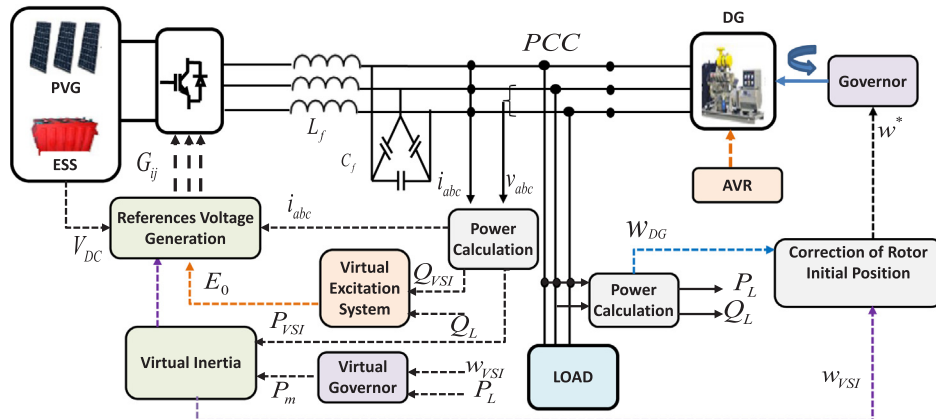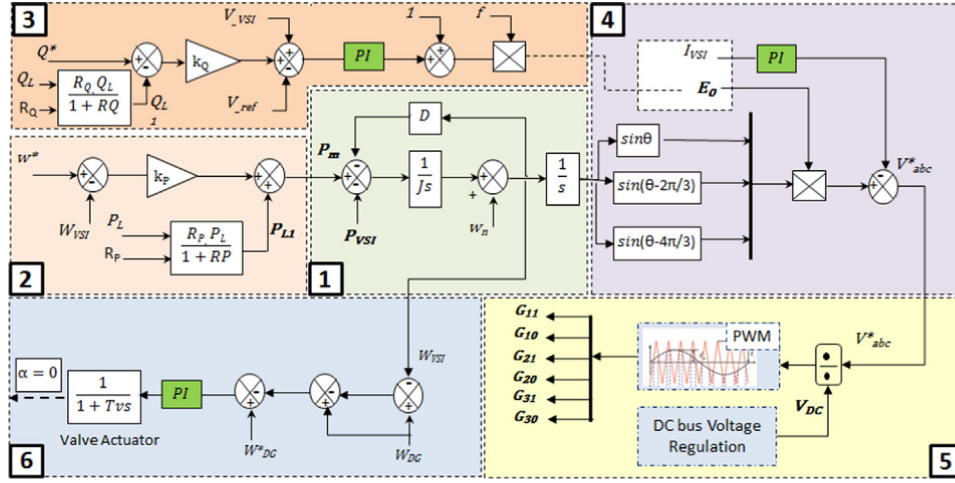

Fig. 8. proposed VSG-based control scheme.

Fig. 9. VSG control scheme: (1) Virtual Inertia, (2) Virtual governor system, (3) Virtual excitation voltage, (4,5) Voltage references generation, (6) Correcting the DG rotor initial position.

$$m = \frac{\omega_{max} - \omega_{min}}{P_{max} - P_{min}} \tag{25}$$

Eq. (24) can be rewritten as follows:

$$\frac{\tau}{m} \frac{d}{dt}(\omega_{VSI} - \omega^*) = (P^* - P_{L1}) - \frac{1}{m}(\omega_{VSI} - \omega^*) \tag{26}$$

By comparing Eq. (26) with the classical second-order swing equation (Eq. (2)), the damp term and inertia term D and J are equivalent to:

$$\begin{cases} D = \frac{\tau}{m} = \frac{P_{max} - P_{min}}{\omega_{max} - \omega_{min}} \\ J = \frac{1}{m} \end{cases} \tag{27}$$

This relation shows on one hand that the system response is slow with a relatively large inertia and quick with a relatively small inertia and on the other hand that the damping coefficient D, is responsible for the low-frequency fluctuation in steady-state. In the proposed control strategy the damping coefficient D must be adjusted according to the desired power ratio R.

3.2.4. Virtual excitation voltage

To keep the VSI output voltage amplitude under control, the droop regulation technique is used for the reactive powers exchange with the DG source.

From Eq. (16), the VSI output reactive power that will be delivered to the load can be written as:

$$V_1 - V \approx x_1 \frac{Q_1}{V_1} \tag{28}$$

The voltage amplitude depends then mainly on the reactive power flow. The following droop control expression can be written as:
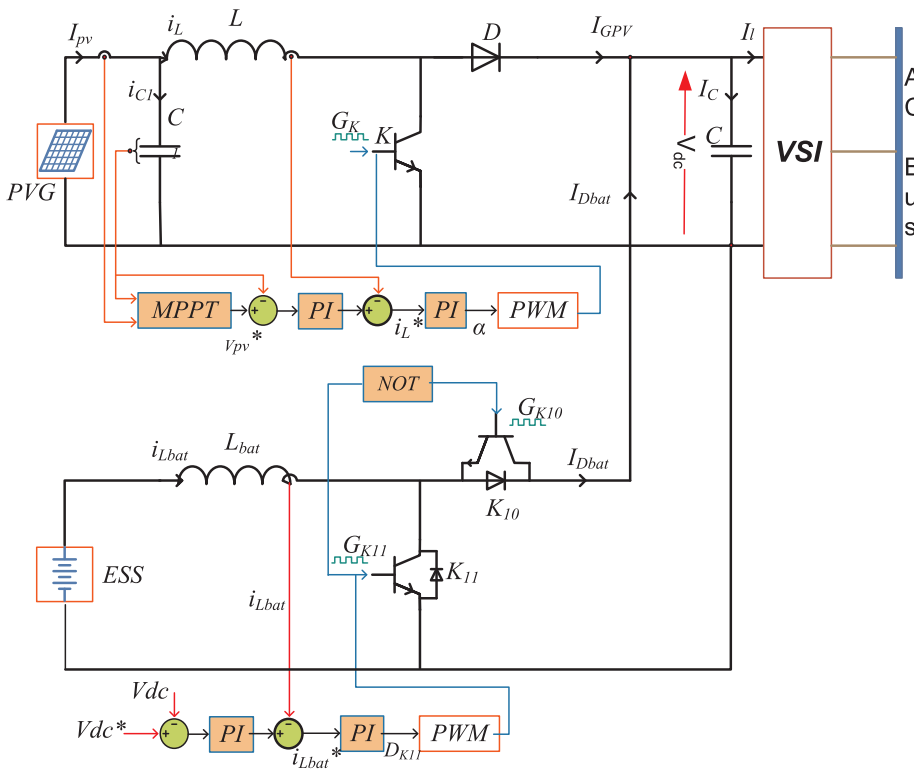
$$(V_{VSI} - V_0) = -k_Q(Q_{VSI} - Q_0) \tag{29}$$

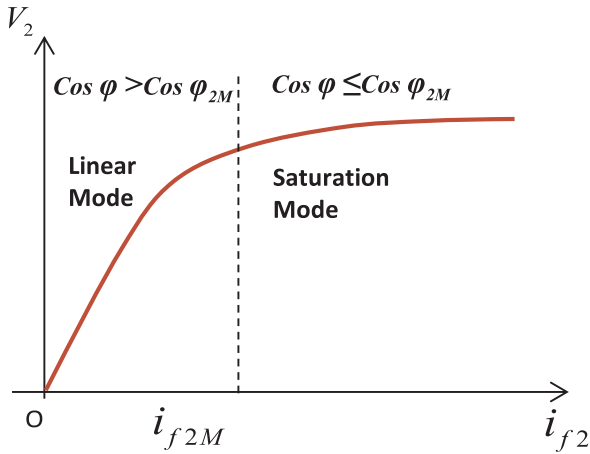**Fig. 10.** V_{dc} voltage regulation.

$$C\frac{d}{dt}(V_{dc}) = i_{PVG} + i_{Dbat} - i_L \tag{35}$$

3.2.6. DG rotor initial position correction

As previously discussed, to ensure the same power sharing between the two sources, it is sufficient to impose a zero-angle of the rotor initial position ($\alpha = 0$). As shown in Part 6 of Fig. 9. This correction can be achieved through an acceleration or deceleration to the DG rotor according to its initial position.

3.3. Problems of Reactive Power Sharing in Hybrid system (PVG-DG)

As discussed in the Introduction Section, the rotor accessibility problem of the DG, influences not only the synchronization process, but also the reactive energy and therefore its sharing with other sources due to the limitation of the AVR. In fact, to regulate the DG output voltage, the AVR maintains the constant voltage up to a certain level by controlling its field winding.

The winding of the rotor field is excited by a direct current i_f. It is through the generated magnetic flux that the AVR compensates the voltage droop or the overvoltage according to the nature of the fed load (inductive or capacitive). Nevertheless this compensation is limited by saturating the magnetic material as shown in Fig. 11. This justifies the $\cos\phi_{2M}$ often marked on the DG nameplate, defined as:

$$\cos\varphi_{2M} = \frac{P_{DG}}{S_{DG}} = \frac{P_2}{S_2} \tag{36}$$

Beyond this value of $\cos\phi_{2M}$, the AVR system is no longer able to maintain the output voltage in term of amplitude.

Due to this limitation of the AVR system, the reactive load sharing cannot fully satisfy Eq. (18).

From a control theory point of view, the design equation of the AVR system is based on the rotor winding geometrical and material parameters. The maximal excitation current i_{fM}, which also corresponds to the maximal flux ϕ_{f2M} and to the maximal excitation voltage V_{f2M}, could be expressed as [33]:

$$i_{f2M} = \frac{k_w a_w}{\rho L_m}\phi_{fM}^2 R_{fM}\frac{1}{v_{f2M}} \tag{37}$$

The geometric, electric, and magnetic parameters of the core and winding window are: the winding window utilization factor K_w; the winding window area a_w; the cooper resistivity ρ; the mean length per turn L_m; and the magnetic reluctance R_{fM}. All these parameters could be replaced with a global core parameter K_n [33]. Eq. (37) can be written as:

$$i_{f2M} = \frac{k_n}{v_{f2M}} \tag{38}$$

The electromotive force V_2 is directly proportional to the reactive component of the excitation current i_f, the actual electrical angular velocity, and the mutual inductance of the stator windings M_f [12].

$$V_2 = \omega M_f i_f \tag{39}$$

Its maximum value is therefore:

$$V_{2M} = \omega M_f i_{f2M} \tag{40}$$

Since there is no saturation in virtual excitation voltage (VEV), the limitation of the AVR system can be compensated by the VEV.

According to the load $\cos\phi$, two possible cases can be distinguished.

- Case 1: When the load $\cos\phi$ is greater than the DG one ($\cos\varphi \geqslant \cos\varphi_{2M}$). Following the proposed control strategy described in Section 3, the active and reactive powers sharing can be achieved according to the desired power ratio ($R = R_P = R_Q$), by imposing a rotor initial position zero-angle ($\alpha = 0$).

Fig. 11. Excitation electromotive force characteristic.

On the other hand, and according to the principle of Synchronous Generator, the excitation electromotive force V_1 can be expressed as:

$$V_1 \approx V + x_{1SR}I_{1q} \tag{30}$$

where I_{1q} and x_{1SR} are the reactive current and the virtual synchronous reactance, respectively.

Let M_{f1} denotes the mutual inductance amplitude of the virtual stator windings, and C denotes the virtual excitation current. Thus the amplitude of the virtual excitation electromotive force can be expressed as [12]:

$$V_1 = \omega M_{f1}i_{f1} \tag{31}$$

If we assume that V_{1B} is the base value of V_1 and i_{f1B} is the base value of i_{f1} (in pu), thus, the virtual excitation voltage and current can be expressed (in pu) as follows:

$$\begin{cases} V_{1*} = \frac{V_1}{V_{1B}} = \frac{\omega M_{f1}i_{f1}}{\omega M_{f1}i_{f1B}} = \omega_* i_{f1*} \\ i_{f1*} = \frac{i_{f1}}{i_{f1B}} = \frac{i_{f1B} + \Delta i_f}{i_{f1B}} = 1 + \Delta i_{f1*} \end{cases} \tag{32}$$

With the VEV, when if changes, the terminal voltage V_1 changes with a very small slope k, and unlike the AVR, the characteristic $V_1 = f(i_{f1})$ is linear (no magnetic saturation). The slope K denotes a voltage adjustment coefficient, which is defined as follows:

$$K = \frac{V_0 - V_1}{V_N} \tag{33}$$

where V_0 and V_1 are the VSI terminal voltages without and with load, respectively and V_N is its rated voltage. Thus, the VEV block diagram is given in Part 3 of Fig. 9. The adopted approach for the calculation of its parameters can be found in [12].

3.2.5. References voltages generation

As shown in Part 4 of Fig. 9, the reference voltages V_{abc}^* are reconstructed by combining the amplitude information E_0 generated by the virtual excitation voltage and the phase information θ generated by the virtual inertia as:

$$\begin{cases} V_a^* = \sqrt{2}E_0 sin\theta \\ V_b^* = \sqrt{2}E_0 sin(\theta - \frac{2\pi}{3}) \\ V_c^* = \sqrt{2}E_0 sin(\theta - \frac{4\pi}{3}) \end{cases} \tag{34}$$

The voltage references thus obtained are divided by the regulated DC bus voltage V_{dc} to generate in the PWM modulation index m, as shown in Part 5 of Fig. 9. As shown by Fig. 10, the ESS is designed to regulate V_{dc}, in order to supply or absorb insufficient or surplus powers. Indeed, the DC bus voltage can be expressed by:

Fig. 12(a) and (b) show the principles of f/P and V/Q droop controls, respectively, for a desired power ratio ($R = 2$). Based on this predefined linear droop characteristic, for a desired active powers sharing ratio ($R_P = 2$), $\omega_{m1} = \omega_{m2}$ can be guaranteed in steady-state. In the same way, to share the reactive power according to the desired reactive powers sharing ratio ($R_Q = 2$), an equal output voltage $V = V_{VSI} = V_{DG}$ is required.

- Case 2: When the load $\cos\phi$ is lower than the DG one ($\cos\varphi < \cos\varphi_{2M}$). The reactive power of the DG must be lower than that of the VSI in order to maintain the above-cited $\cos\phi$ condition, whatever the reactive power required by the load.

Fig. 13 show the principle of V/Q droop control when $\cos\varphi < \cos\varphi_{2M}$. In this case, the desired power ratio R must be imposed according to Q_{2M}, in order to prevent the AVR operation in its saturation area. It can therefore be expressed as follows:

$$R = R_P = R_Q = \frac{Q_1}{Q_{2M}} = \frac{Q_L}{Q_{2M}} - 1 \qquad (41)$$

4. Simulation results

In this section, the effectiveness of the proposed VSG-based control strategy, is evaluated by simulating the hybrid power system described in Fig. 2 with the parameters given in Table 1.

The functional behavior of the system energy sources as well as the synchronization process between the VSI and the DG are illustrated in this section by means of numerical simulation of a few relevant cases. The electrical load comprises both resistive and inductive components that are connected in parallel to the AC bus as shown in Fig. 2. Based on the proposed control strategy, the desired power ratio is fixed to $R = R_P = R_Q = 2$. In this case, the synchronization between the VSI and the DG is guaranteed since ($\omega_1 = \omega_2 = \omega$) and ($V_1 = V_2 = V$) in steady-state, as described by Fig. 12(a) and (b).

The simulation is divided into several time intervals to evaluate the dynamic performance of the VSI, DG, PVG, and ESS under loading transitions. Initially, the system operates with load1, then load2 is connected at $t = 1s$ before cutting-off from the system at $t = 2s$.

The active and reactive powers dynamic responses are shown in Fig. 14(a) and (b), respectively. It is clear that during the three simulation steps ($0 < t < 1s$, $1 < t < 2s$, and $2 < t < 3s$), the two sources (VSI and DG), share respectively ratio of 2/3 and 1/3 of the active and reactive powers requested by the load. The desired active and reactive power sharing between the two sources is obtained because the ratios are the same, as discussed in Section 3. In this case, $P_{VSI} = 2P_{DG} = 2/3P_{load}$ and $Q_{VSI} = 2Q_{DG} = 2/3Q_{load}$. It can also be observed that a transient regime appears at the beginning of the two sources synchronization. This transient regime is due to the DG required time to correct its initial position by imposing $\alpha = 0$, as explained in Section 3.2.6.

Fig. 15(a) illustrate the output voltages at PCC. It can be observed
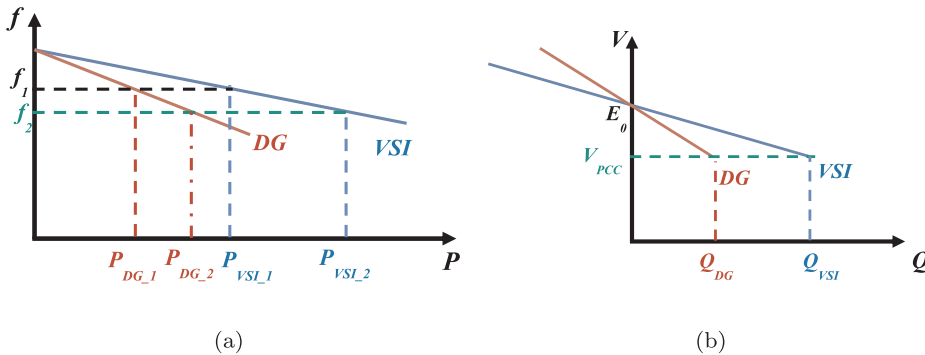
Fig. 13. V/Q droop controls for $\cos\varphi \leqslant \cos\varphi_{2M}$.

Table 1
Simulation parameters.

PVG Parameters		DG Parameters	
PVG RP	3.2 kW	DG RP	10 KVA
Panel RP	135 W	τ_1	0.03 sec
ns	9	τ_2	0.05 sec
np	4	ka	2.7
T	25°	r_2	0.6Ω
a	1.3	x_2	5 mH
ESS Parameters		VSI Parameters	
V_{bat}	12 V	r_1	0.6Ω
C_{bat}	150 Ah	x_1	5 mH
r_{bat}	1 Ω	C_f	0.033 mF
L_{bat}	0.05 H	L_f	0.048 mH

that the AC voltage is not influenced by the load changes. Both AVR and VEV systems compensate the voltage drop due to the reactive power of each source ($Q_{VSI} = 2Q_{DG} = 2/3Q_{load}$). Moreover, the DG rotor initial position correction can be clearly observed in the zoom of the AC voltage depicted by Fig. 15(b).

Fig. 16(a) and (b) show the battery currents and the PVG output power, respectively. It can be noticed that when the load current is higher than the PVG one, the ESS is therefore in the discharging state ($I_{bat} > 0$) and when the load current increases, the ESS moves to the charging state ($I_{bat} < 0$).

The frequency dynamic performance at PCC during the loading transition is ullistred by Fig. 17(a). It can be observed that the DG frequency deviations are compensated by the VSI frequency ones, in order to keep a constant frequency, which means that the VSI provides a virtual inertia to the system to allow a better stability.

Fig. 17(b) is provided to highlight the DC bus voltage regulation by an ESS through a buck-boost converter as described in Fig. 10. It can be noticed that the DC bus voltage is not affected by the load variation and it is well regulated at 650 V, therefore proving the performance of the proposed control.
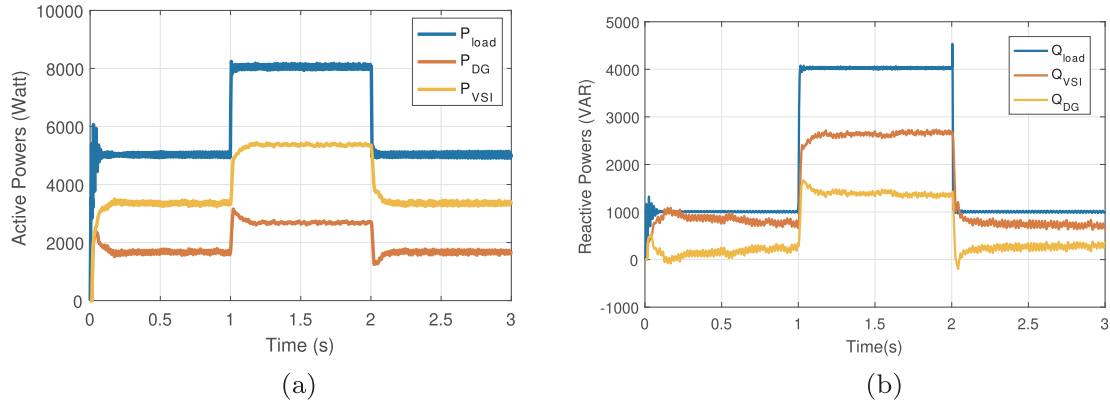
(a)

(b)

Fig. 12. Droop controls for $R = 2$. (a) f/P droop control, (b) V/Q droop control.

Fig. 14. Powers sharing simulation results. (a) Active power, (b) Reactive power.

5. Experimental results

Real-time experiments are carried out using the PCI 6281 card controller board with input/output interface. Fig. 18 shows the developed experimental test bench and its main components. The synchronization process and power sharing method control blocks are implemented on a reduced-scal test bench, to show the practical feasibility of the proposed VSG-based control strategy. However, it should be mentioned that due to DG unavailability and difficulty for indoor use, a second VSI is used for emulation purposes. Its virtual mechanical parameters correspond to those of a DG with a rated power of 10 kVA.

Experimental tests were carried out for two cases. In the first case, the second VSI is connected during a very precise time interval in order to illustrate the synchronization process, while in the second case the two VSIs are connected in parallel in order to evaluate the practical feasibility of the power sharing between the two power sources according to the desired power ratio R.

5.1. Synchronization process experimental validation

In order to illustrate the synchronization process between the two voltage source inverters VSI$_1$ and VSI$_2$, the load power is initially provided by VSI$_1$, after that, the VSI$_2$ is connected at $t = 5s$ before cutting off from the system at $t = 25s$.

The test has been carried out for a purely resistive load with a desired power ratio $R = P_1/P_2 = P_1/P_2 = 1/2$. At the instant of connection of the second inverter VSI_2, the output voltages V_1 and V_2 are not superimposed.

As discussed in Section 3.2.6, the correction of the initial position can be achieved through an acceleration/deceleration of the virtual DG rotor. The synchronization can be ensured by the correction of the VSI$_2$ virtual rotor initial position by imposing a zero-angle ($\alpha = 0$) through

the reconstruction of the reference voltages as follows:

$$\begin{cases} V_{a2}^* = \sqrt{2} E_{02} sin(\theta - \alpha) \\ V_{b2}^* = \sqrt{2} E_{02} sin(\theta - \frac{2\pi}{3} - \alpha) \\ V_{c2}^* = \sqrt{2} E_{02} sin(\theta - \frac{4\pi}{3} - \alpha) \end{cases}$$

(42)

From the experimental results depicted in Fig. 19–22, it can be clearly seen that after the second VSI connection, the load power is shared between the two VSIs, according to the desired power ratio $R = 1/2$. In fact, the first provides $1/3P_{load}$ while the second provides $2/3P_{load}$. The microgrid consists in this case of two grid-forming power converters connected in parallel and controlled in closed-loop to work as ideal AC voltage sources with a given amplitude $V_{max} = 28$ V and frequency $f = 50$ Hz. As voltage sources, they present a low-output impedance. The currents flowing through their output impedances are expressed as:

$$I_{VSI2} = 2I_{VSI1} = \frac{2}{3}I_{Load}$$

(43)

The virtual excitation voltage (V_{f2}) of VSI$_2$ must be greater than V_{f1} in order to compensate the voltage drop (see Section 3.2.4). The virtual electromotive forces are not the same ($V_1 > V_2$) and can be expressed as follows:

$$\begin{cases} V_1 = V_{Load} + \sqrt{r_1^2 + x_1^2} \frac{I_{Load}}{3} \\ V_2 = V_{Load} + \sqrt{r_2^2 + x_2^2} \frac{2I_{Load}}{3} \end{cases}$$

(44)

From Fig. 23 and although the test was performed for a purely resistive load, a reactive powers oscillation occurs during the connection and disconnection of the second VSI. Besides, active power control is not independent from the reactive power one, as a change of the active power set value at 5s and 25s, also causes a transient change in reactive
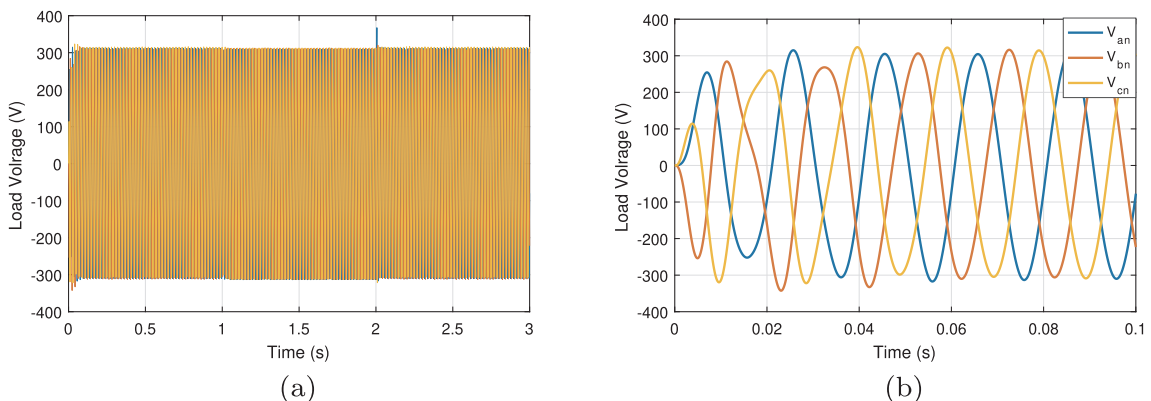

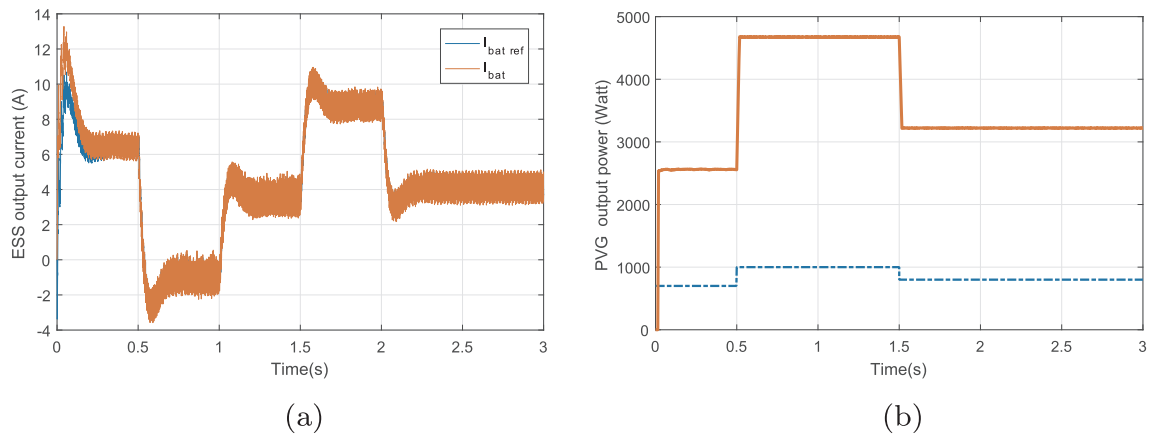**Fig. 15.** Simulation results in AC bus. (a) Output voltages at PCC, (b) Zoom of output voltages.

(a)   (b)

Fig. 16. Simulation results in DC bus. (a) ESS output current, (b) PVG output Power.
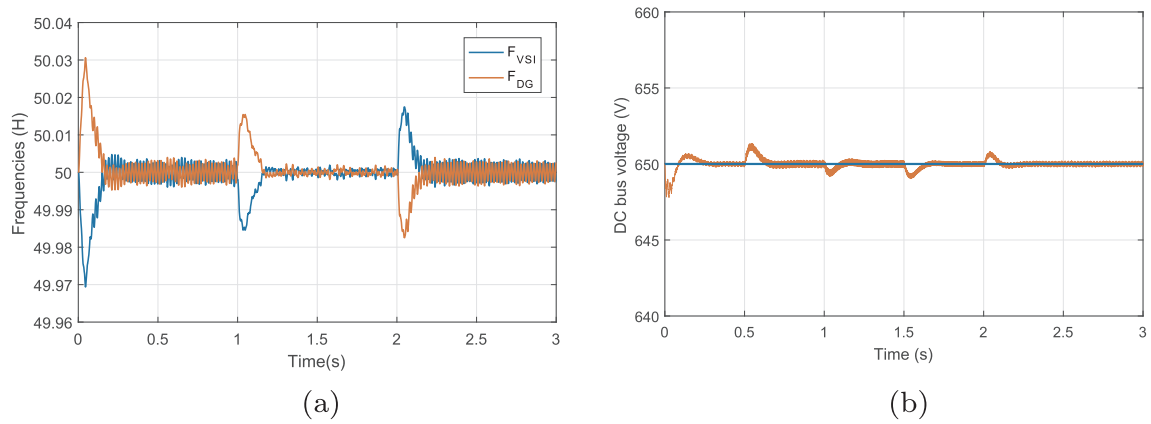

(a)   (b)

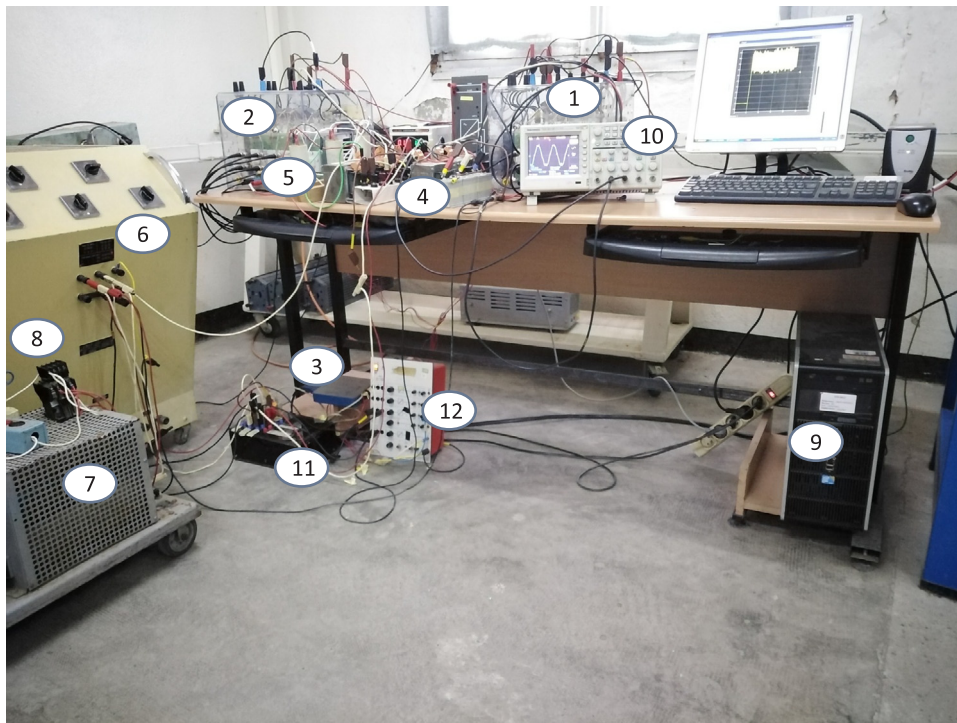**Fig. 17.** (a) Frequency at PCC, (b) DC bus voltage.

Fig. 18. Experimental test bench. (1) VSI1, (2) VSI2, (3) PCI 6281 card controller board with input/output interface, (4) LC filter 1, (5) LC filter 2, (6) Resistive load, (7) Inductive load, (8) load switch, (9) PC, (10) Scope, (11) Current measurement, (12) Voltage measurement.
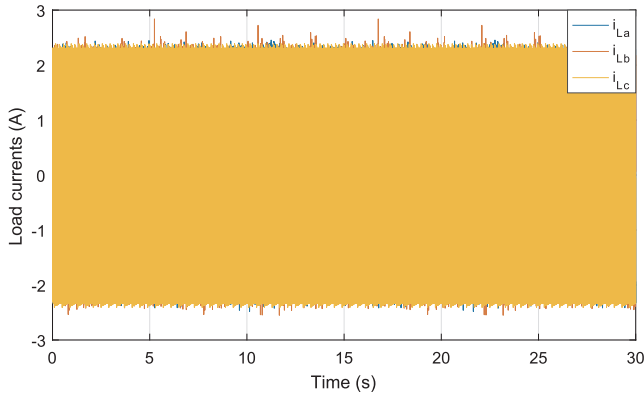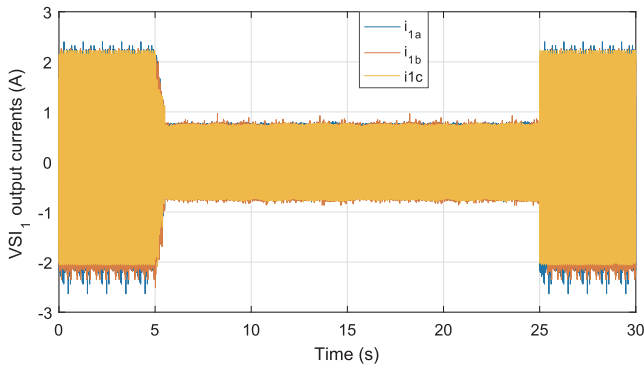
Fig. 19. Load currents.

Fig. 20. VSI1 output currents.
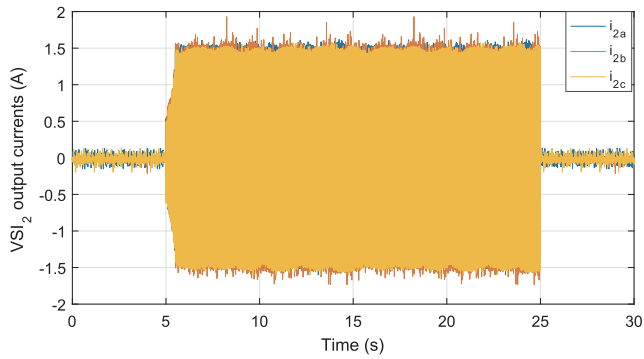
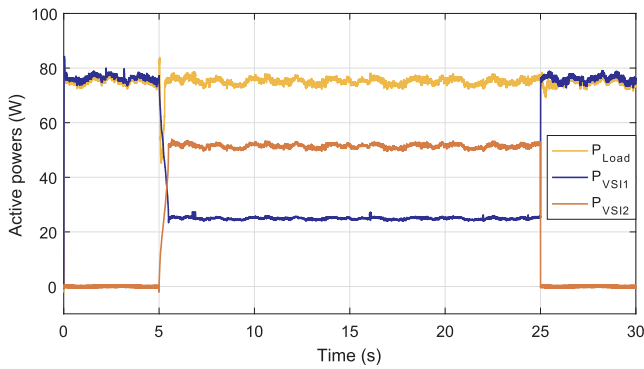**Fig. 21.** VSI2 output currents.
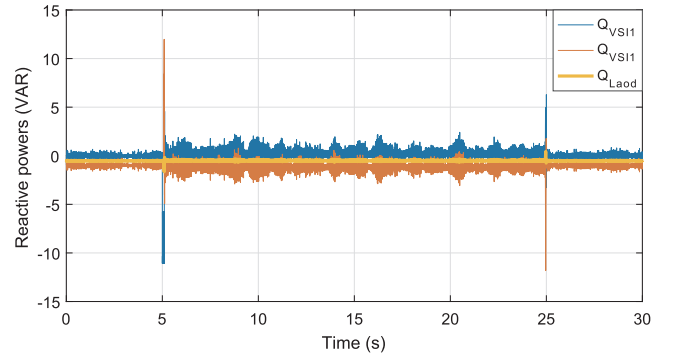

Fig. 22. Active power sharing.

Fig. 23. Reactive power sharing.
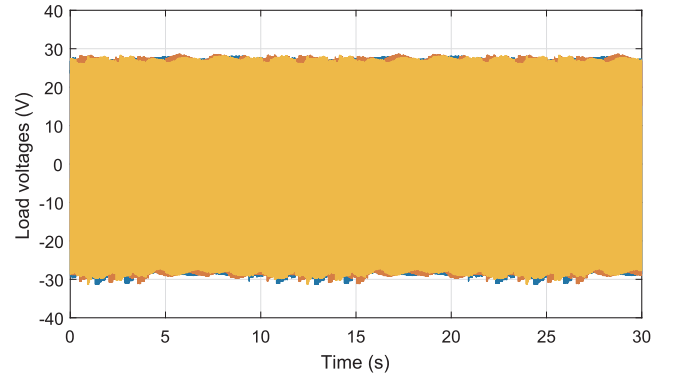
Fig. 24. Output voltages in AC bus.

Table 2
Experimental validation parameters.

VSI$_1$ Parameters		VSI$_2$ Parameters	
Parameter	Value	Parameter	Value
r_1	3.8Ω	r_2	3.8Ω
x_{R1}, x_{R2}, x_{R3}	10, 20, 26 mH	x_2	10 mH
$cf_{R1}, cf_{R2}, cf_{R3}$	50, 100, 330 µF	c_f	30 µF
J_1	0.22 kg m^2	J_2	0.06 kg m^2
D_{R1}, D_{R2}, D_{R3}	2, 4, 6	D_2	2
K_{Q1}	0.0001	K_{Q2}	0.0001
K_{p1}	1000	K_{p2}	2000

power sharing. In fact, Low-voltage microgrid lines present resistive properties (neglected in the proposed control strategy), which can lead to a strong coupling between active and reactive experimental power outputs. Here and in order to compensate the uneven line voltage drop of the two VSIs, an adequate sizing of VSI$_1$ filter ($x_1 = 2x_2$) can enormously reduce the coupling oscillations.

It can be observed also from Fig. 24, that the voltage at PCC is well regulated, which clearly mean that the proposed VSG-based control strategy is able to synchronize the two VSI$_s$ without PLL. Note here that high-frequency oscillations can be observed in the output currents and voltages, despite the use of a first-order low pass filter for output currents and voltages measurement. This is due to a practical constraint related to the LC filters sizing, which has been carried out according to the laboratory available inductance and capacitor (Table 2).

5.2. Power sharing method experimental validation

In this part, the two VSIs are connected in parallel in order to evaluate the practical feasibility of the proposed power sharing, according to the desired power ratio *R*. Initially, the system operates with the first load then the second load is connected at $t = 10s$ before cutting
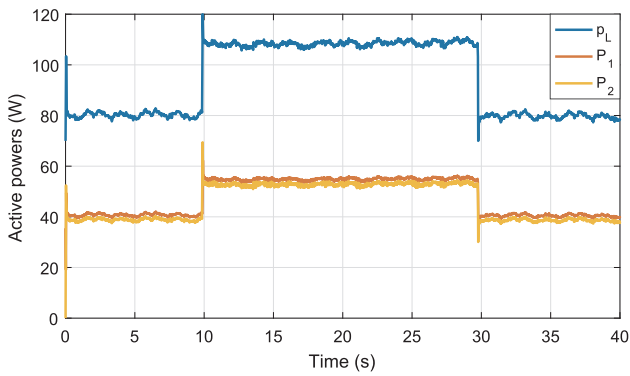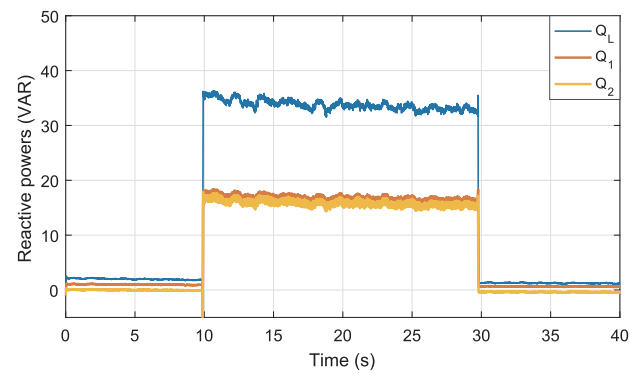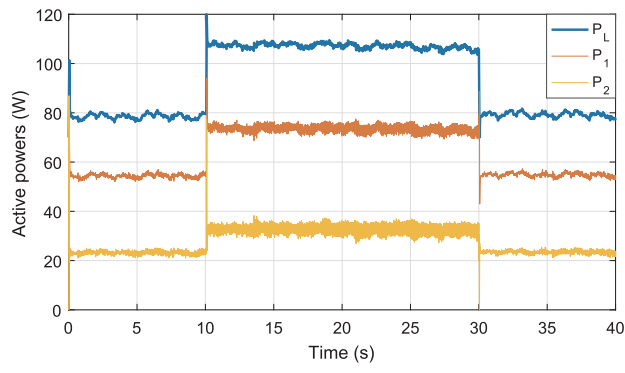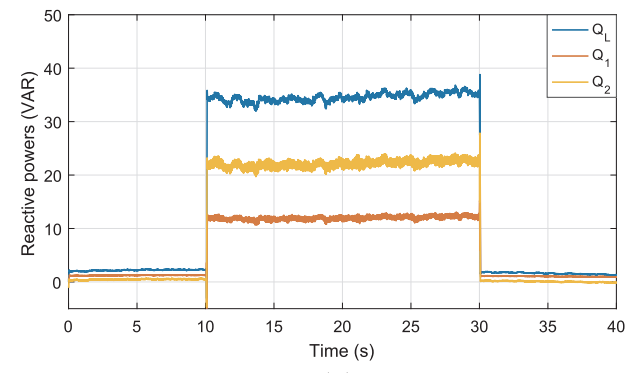
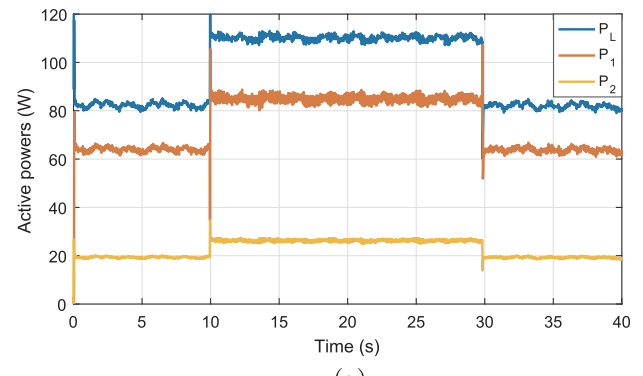Fig. 25. Experimental power sharing result for $R = 1$. (a) Active power sharing, (b) Reactive power sharing.
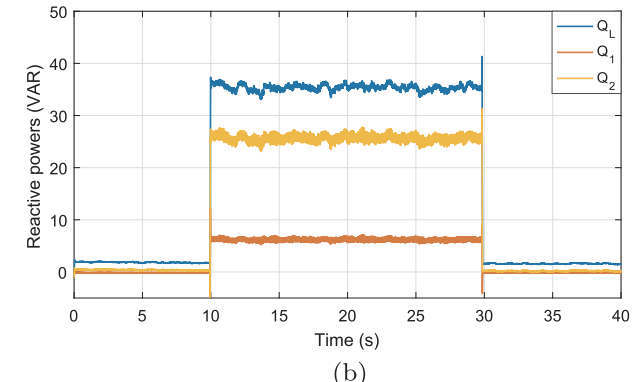

Fig. 26. Experimental power sharing result for $R = 3$. (a) Active power sharing, (b) Reactive power sharing.

Fig. 27. Experimental power sharing result for $R = 3$. (a) Active power sharing, (b) Reactive power sharing.

off from the system at $t = 30s$.

Figs. 25–27, corresponds to a desired power ratio of $R = 1$, 2, and 3, respectively. In each test, the waveforms from top to down are the load active power, VSI$_1$ output active power, VSI$_2$ output active power, load reactive power, VSI$_1$ output reactive power, and VSI$_2$ output reactive power, respectively.

These achieved results clearly show that the two VSIs contribute to the load power demand by a set beforehand power ratio. Again, they validate the effectiveness of the proposed power sharing method. In fact, by applying the VSG control, the active and reactive powers are shared according to the desired power ratios of VSI$_1$ and VSI$_2$.

In order to improve the system stability, the virtual inertia J and the damping coefficient D must be judiciously chosen. The system response is slow with a relatively large inertia and quick with a relatively small inertia. It is strongly emphasized that the practical value of the virtual inertia of VSI$_1$ ($J1 = 0.22$, given in Table 2) has been chosen for a better system stability; while the practical value of the virtual inertia of VSI$_2$ ($J2 = 0.06$, given in Table 2) has been chosen corresponding to the diesel generator parameters. While the damping coefficients ($D1_{R1} = D2$, $D1_{R2} = 2D2$, $D1_{R3} = 3D2$) have been adjusted according to the desired active power ratio R, as discussed in Section 3.2.3.

6. Conclusion

In this paper, a new virtual synchronous generator-based control strategy has been proposed for a hybrid PV-Diesel power system in a stand-alone context. The control idea aims to synchronize the VSI and the DG without a PLL and with correction of the diesel generator rotor initial position. In the proposed approach, the active and reactive powers sharing between the two energy sources can be envisaged with a desired ratio.

Simulations and experiments under load variation have successfully proved the effectiveness of the proposed virtual synchronous generator-

based control strategy. It has been particularly demonstrated that the proposed control ensures synchronism and achieves powers sharing according to the desired power ratio.

Declaration of Competing Interest

The authors declare that they have no known competing financial interests or personal relationships that could have appeared to influence the work reported in this paper.

References

[1] Kim Y-S, Kim E-S, Moon S-I. Frequency and voltage control strategy of standalone microgrids with high penetration of intermittent renewable generation systems. IEEE Trans Power Syst 2016;31(1):718–28.

[2] Belila A, Benbouzid M, Berkouk E-M, Amirat Y. On energy management control of a pv-diesel-ess based microgrid in a stand-alone context. Energies 2018;11(8):2164.

[3] Tawil TE, Benbouzid JFCM, Yao G. Design, analysis, and comparison of inverter control methods for microgrid application for stand-alone sites. 2017 IEEE international electrical machines and drives conference. 2017. p. 1–6.

[4] Alipoor J, Miura Y, Ise T. Power system stabilization using virtual synchronous generator with alternating moment of inertia. IEEE J Emerg Sel Top Power Electron 2015;3(2):451–8.

[5] Lu L, Chu C. Consensus-based secondary frequency and voltage droop control of virtual synchronous generators for isolated ac micro-grids. IEEE J Emerg Sel Top Circ Syst 2015;5(3):443–55.

[6] Bevrani H, Ise T, Miura Y. Virtual synchronous generators: A survey and new perspectives. Int J Electr Power Energy Syst 2014;54:244–54.

[7] Zhang B, Yan X, Li D, Zhang X, Han J, Xiao X. Stable operation and small-signal analysis of multiple parallel dg inverters based on a virtual synchronous generator scheme. Energies 2018;11(1). https://doi.org/10.3390/en11010203.

[8] Zhao H, Yang Q, Zeng H. Multi-loop virtual synchronous generator control of inverter-based dgs under microgrid dynamics. IET Generat Transmiss Distrib 2017;11(3):795–803. https://doi.org/10.1049/iet-gtd.2016.0645.

[9] Tawil TE, Yao G, Charpentier JF, Benbouzid MEH. Design and analysis of a virtual synchronous generator control strategy in microgrid application for stand-alone sites. IET Generat Transmiss Distrib 2019:1–8.

[10] Wu W, Chen Y, Luo A, Zhou L, Zhou X, Yang L, et al. A virtual inertia control strategy for dc microgrids analogized with virtual synchronous machines. IEEE Trans Industr Electron 2017;64(7):6005–16.

[11] Gao C, Liu X, Chen H. Research on the control strategy of distributed energy resources inverter based on improved virtual synchronous generator. Tech. Rep., in matworks models; 2017.

[12] Yao G, Lu Z, Benbouzid M, Tang T, Han J. A virtual synchronous generator based inverter control method for distributed generation systems. In: IECON 2015–41st Annual Conference of the IEEE Industrial Electronics Society; 2015, p. 002112–002117. https://doi.org/10.1109/IECON.2015.7392413.

[13] Xu H, Zhang X, Liu F, Shi R, Yu C, Cao R. A reactive power sharing strategy of vsg based on virtual capacitor algorithm. IEEE Trans Industr Electron 2017;64(9):7520–31.

[14] Li B, Zhou L. Power decoupling method based on the diagonal compensating matrix for vsg-controlled parallel inverters in the microgrid. Energies 2017;10(12):2159.

[15] Han Y, Li H, Shen P, Coelho EAA, Guerrero JM. Review of active and reactive power sharing strategies in hierarchical controlled microgrids. IEEE Trans Power Electron 2017;32(3):2427–51.

[16] Altahir SY, Yan X, Gadalla AS. Active and reactive power sharing control strategy for vsgs in microgrid considering the different capacities of distributed energy resources. IET Cyber-Phys Syst: Theory Appl 2018;3(3):167–73.

[17] Liu J, Miura Y, Bevrani H, Ise T. Enhanced virtual synchronous generator control for parallel inverters in microgrids. IEEE Trans Smart Grid 2017;8(5):2268–77.

[18] Chen D, Xu Y, Huang AQ. Integration of dc microgrids as virtual synchronous machines into the ac grid. IEEE Trans Industr Electron 2017;64(9):7455–66.

[19] Alipoor J, Miura Y, Ise T. Stability assessment and optimization methods for microgrid with multiple vsg units. IEEE Trans Smart Grid 2018;9(2):1462–71. https://doi.org/10.1109/TSG.2016.2592508.

[20] Serban I, Ion CP. Microgrid control based on a grid-forming inverter operating as virtual synchronous generator with enhanced dynamic response capability. Int J Electr Power Energy Syst 2017;89:94–105.

[21] Datta M, Senjyu T, Yona A, Funabashi T, Kim C. A frequency-control approach by photovoltaic generator in a pv–diesel hybrid power system. IEEE Trans Energy Convers 2011;26(2):559–71. https://doi.org/10.1109/TEC.2010.2089688.

[22] Choopani M, Hosseinain S, Vahidi B. A novel comprehensive method to enhance stability of multi-vsg grids. Int J Electr Power Energy Syst 2019;104:502–14.

[23] Hirase Y, Abe K, Sugimoto K, Sakimoto K, Bevrani H, Ise T. A novel control approach for virtual synchronous generators to suppress frequency and voltage fluctuations in microgrids. Appl Energy 2018;210:699–710.

[24] Bose U, Chattopadhyay SK, Chakraborty C, Pal B. A novel method of frequency regulation in microgrid. IEEE Trans Ind Appl 2019;55(1):111–21.

[25] Farrokhabadi M, Cañizares CA, Bhattacharya K. Frequency control in isolated/islanded microgrids through voltage regulation. IEEE Trans Smart Grid 2017;8(3):1185–94. https://doi.org/10.1109/TSG.2015.2479576.

[26] Belila A, Tabbache B. A control strategy of hybrid system "diesel-photovoltaic-battery" for stand-alone applications. 2015 IEEE 15th international conference on environment and electrical engineering (EEEIC) 2015. p. 860–5. https://doi.org/10.1109/EEEIC.2015.7165276.

[27] Belila A, Tabbache B, Berkouk E, Benbouzid M. Integration of a storage system in a hybrid system diesel-photovoltaic for stand-alone applications. In: 2017 IEEE International Conference on Environment and Electrical Engineering and 2017 IEEE Industrial and Commercial Power Systems Europe (EEEIC/ICPS Europe); 2017. p. 1–6. https://doi.org/10.1109/EEEIC.2017.7977884.

[28] Rocabert J, Luna A, Blaabjerg F, Rodríguez P. Control of power converters in ac microgrids. IEEE Trans Power Electron 2012;27(11):4734–49.

[29] Chen M, Xiao X. Hierarchical frequency control strategy of hybrid droop/vsg-based islanded microgrids. Electric Power Syst Res 2018;155:131–43.

[30] D'Arco S, Suul JA, Fosso OB. A virtual synchronous machine implementation for distributed control of power converters in smartgrids. Electric Power Syst Res 2015;122:180–97.

[31] Gao C, Liu X, Chen H. Research on the control strategy of distributed energy resources inverter based on improved virtual synchronous generator. Sci Rep 2017;7(1):9025.

[32] Hou X, Sun Y, Zhang X, Lu J, Wang P, Guerrero JM. Improvement of frequency regulation in vsg-based ac microgrid via adaptive virtual inertia. IEEE Trans Power Electron 2019. https://doi.org/10.1109/TPEL.2019.2923734. [Early Access].

[33] Amodeo HGC, Santiago J, Oliva AR. High-performance control of a dc-dc z-source converter used for an excitation field driver. IEEE Trans Power Electron 2012;27(6):2947–57.